Applied Computer Science, vol. 18, no. 3, pp. 86–104
doi: 10.35784/acs-2022-23

Submitted: 2022-06-15 | Revised: 2022-08-17 | Accepted: 2022-09-24

Keywords: Computational Fluid Dynamics, PM Pollution, Propeller Aerodynamics, Multi-rotor Robot Design

Grzegorz SUCHANEK [0000-0003-0294-3574]*, *Roman FILIPEK* [0000-0003-4763-023X]**

COMPUTATIONAL FLUID DYNAMICS (CFD) AIDED DESIGN OF A MULTI-ROTOR FLYING ROBOT FOR LOCATING SOURCES OF PARTICULATE MATTER POLLUTION

Abstract

The use of flying robots for various environmental protection issues is a very important and current research topic. Designing a dedicated multi-rotor flying robot is necessary for the efficient and automated localization of sources of air pollution, especially solid particles. In particular, one of the most important requirements that must be met by such a robot is its appropriate impact on the measurement process, i.e., increasing the sensitivity of sensors or reducing the interference. This is particularly difficult because its rotating rotors introduce significant disturbances to the surrounding fluid. In these studies, the design process is supported by the creation of a mathematical flow model and a series of analyzes to optimize the PM measurement system. The model is built using the finite-volume method in ANSYS Fluent software and steady-state RANS averaging. First, a flow field model with one propeller was modeled and its parameters identified by comparison with the results from the dedicated original dynamometer stand -- characteristics of the propeller performance. On the basis of the simulations and measurement of one rotor, subsequent systems of the highest practical importance are built. The effect of that design process was the preparation and testing of a functional robot prototype. The field parameter distributions resulting from the analyzes, in particular the turbulence intensity, allow one to propose a criterion on the basis of which both the best rotor configuration and localization of sensors are selected.

1. INTRODUCTION

Human health and life, especially under urban conditions, are constantly exposed to the adverse effects of polluted air. It is responsible for the prevalence of various types of allergies or other diseases, including cancer. Decaying building facades can also be included here as less obvious environmental damages. High concentrations of solid particles pose

* AGH University of Science and Technology, Faculty of Mechanical Engineering and Robotics, Department of Power Systems and Environmental Protection Facilities, Krakow, Poland, suchanek@agh.edu.pl
** AGH University of Science and Technology, Faculty of Mechanical Engineering and Robotics, Department of Power Systems and Environmental Protection Facilities, Krakow, Poland, roman.filipek@agh.edu.pl

a particular threat. Therefore, there is a constant need to find and develop solutions that would allow to locate the sources of this type of pollution. The sources of this type include, among others, wildfires or other processes in which low-quality fuels or waste are incinerated.

Particle concentration data collection methods can be mainly divided into stationary or mobile methods. Stationary methods use a fixed measurement grid, which are stationary meteorological stations. However, nowadays the most important are mobile methods utilizing flying robots, in particular multi-rotor robots. The use of such a robot requires complex analysis, as rotating rotors of a multirotor robot during operation introduce a large disturbance into the natural field of air flow and gases that carry the particulate matter, thus disrupting the process of their measurement.

Measurements can be made directly during flight when the robot is equipped with appropriate sensors. However, that approach is limited only to the capabilities of usually low-cost, lightweight sensors that can be mounted on the robot. In cases where the robot's task is to locate the source of the pollution, the accuracy of the sensor is less important. The other option is to build robots where the robot is not equipped with an analyzer but with an air sampling system. The air is taken into special tanks or bags, and the composition analysis is carried out on the ground after landing. An example of such work can be (Chen et al., 2018; Cheng et al., 2019). An air intake system (Cheng et al., 2019), dedicated to the extraction of volatile organic compounds (VOCs), has been attached to a telescopic shaft to keep the system inlet away from the powerful air flow from the propellers. In this case, a measuring system was used in the form of a special thin tube (needle trap sampler). It has been shown to be a better solution than a stainless-steel air tank or teflon bags. The results were verified under controlled conditions. The optimal inlet location was determined using *SolidWorks* software. The work (Dieu Hien et al., 2019) presents an overview of the available methods for sampling volatile organic compounds. These solutions eliminate the problems of low accuracy of sensors placed directly on the robot. Due to the desirable features of low empty weight, such sensors do not have measurement properties similar to stationary devices used in laboratories. However, in this case, it is not possible for the robot to use the data on an ongoing basis, and thus, i.e., automatic locating the sources of maximum pollution concentration (Suchanek, Wołoszyn & Gołaś, 2022).

Measurements of solid particles using multirotor robots have been described in many articles (Chiang et al., 2020, Chang; Chen & Huang, 2018; Landolsi et al., 2018). More advanced studies are: (Wang, 2019) where the vertical profile, incl. $PM_{2.5}$ particles and O_3 ozone were determined at heights up to 140 m (Mayuga et al., 2018), where the measurements carried out in the city during heavy traffic with the use of a quadcopter robot were presented. A simple recorder based on the Arduino platform was mounted under the robot, equipped with a: temperature, humidity, and a particulate matter sensor. In (Chunithipaisan et al., 2018) a similar simple system is presented, also based on the Arduino platform. Three-dimensional graphs of measured values for exemplary flights are presented. In the work (Gu, Michanowicz & Jia, 2018) a modular system was proposed, and sample measurements of PM2.5 and NO_2 were presented. The purpose of the study (Alvarado et al., 2017) was to develop a methodology to monitor PM10 dust particles produced as a result of mining activities. An aerodynamic experiment was carried out in which the robot was placed on a 2.5 m high pole and measurements were made using an anemometer. On the basis of the measurements, a three-dimensional map of the air flow around the robot was generated,

and it was decided to place the measurement system inlet on the raised platform, about 50 cm above the robot. An analysis of the optimal hover time is also presented. Too short time (and therefore measurement) is undesirable as it increases the measurement errors. On the other hand, too long time reduces the number of possible measuring points. The article (Villa et al., 2016) presents a similar study in which air flow around a hexacopter robot was investigated. The tests were carried out using a manual anemometer, the position of which was tracked by the *VICON* system (Vicon Motion System Ltd., Oxford, UK). This system allows tracking and locate the position and orientation of an object in a room. In addition to the particle detector, the use of CO_2, CO, NO_2, NO gas sensors were also assessed to evaluate the possible performance of a robot-based flying measurement system of diesel engine emissions. On the basis of the conducted research, some design guidelines were indicated, including: the best solution is to mount the sensors on the extended arm at a distance of about 1–1.2 m from the robot's center, and the propellers cause a thinning effect, which manifests itself as a decrease in the gas concentration indicated by sensors mounted closer to the center of the robot.

The study (Wang et al., 2020) focused on the analysis and determination of the vertical profile of the distribution of solid particles. The six-rotor robot was equipped with a *AM510* $PM_{2.5}$ sensor. Measurements were made at heights of up to 1000m. The advantages and disadvantages of various measurement methods of particulate matter, such as ground station, meteorological tower, tethered balloon, ground *LiDAR*, satellite remote sensing, as well as manned and unmanned aerial vehicles, are also discussed. In the case of an unmanned vessel, it is necessary to take appropriate safety measures by avoiding airport zones and crowded communities and avoiding measurements in extreme weather conditions. Measurements were made at several different times of the day. The influence of temperature and humidity on the vertical distribution of solid particles is also discussed. Attention was paid to the problem of verifying the accuracy of measurements made with the use of a flying robot, therefore comparative measurements were carried out with a tethered balloon. It was indicated that it is necessary to reduce the influence of turbulent flow around the robot by appropriate localization of the inlet of the measuring system.

The work aimed at analyzing and describing the air movement around the robot includes (Burgués et al., 2019), presenting a small commercial *Crazyflie 2.0* nanoquadrocopter, weighing only 27 g. The use of such a robot is therefore limited to closed rooms and low wind speeds. The work shows visualization of aerodynamic phenomena around the robot in the wind tunnel. The work (Ni et al., 2017) concerns the monitoring of crops using a multi-rotor robot. For this purpose, advanced research was performed in the *ANSYS* environment of the *Phantom* commercial robot from *DJI*. Both the propeller and the entire robot were scanned with a 3D scanner. A non-structural mesh was used for the analysis. Based on the results obtained, it was established that two multispectral sensors of crop growth should be placed at the ends of a 1.5 m symmetrical extended arm. The measurement data are analyzed at the ground station. The paper (Luo et al., 2016) presents a numerical model for dynamic simulation of dispersion under the influence of propeller motion. The study (Smith et al., 2016) uses smoke to visualize the aerodynamic phenomena around a robot with four rotors. (Nagy & Jahn, 2019) uses the approach of placing the sensors on a symmetrical boom. A commercial robot and a self-built measuring system are used to measure wind farms.

The paper (Parra et al., 2018) analyzes the aerodynamic disturbances caused by the operation of a six-rotor robot equipped with propellers with two or four blades. However,

the work did not analyze the forces, torques, or power generated for the options analyzed. Preliminary research, where the CFD model was verified on the basis of measurements on the dynamometer stand were presented in (Ciesielka & Suchanek, 2019). In this paper, modelling and simulation of the robot prototype with four rotors were also carried out. The work (Faraz et al., 2020) modeled the flow field around a robot with four rotors. In the tests, the generated thrust force of the robot's propeller was determined for different rotational speeds of the rotor, which allowed the determination of an unknown rotor thrust constant. Based on the research, it was found that the analyzed propeller is able to generate the necessary thrust to lift the robot and can withstand a dynamic load without failure. However, the research conducted was not compared with the data from the experiment.

The article (Hutchinson, Liu & Chen, 2019) generally summarizes the problems of optimal placement of the measuring system, i.e., the influence of the rotors on the dispersion of the measured gas concentration and the overall operation of the sensors. As mentioned above, as well as in this article, it was indicated that this effect was taken into account and various studies were carried out in order to determine the optimal position for the measuring system. Various solutions were considered: under the rotors of the robot, in its center, either elevated above or below the platform, between the rotors, or on the boom. As the authors point out, on the basis of simulations *CFD*, smoke visualizations or pressure and flow measurements on the rotors carried out in various studies, certain conclusions can be drawn, despite contradictory results. The general consensus is that the robot has a negative influence on the measuring system: the results of gas concentration measurements are underestimated and their uncertainty increases. The most accurate measurements can be obtained from a sensor located outside of the area disturbed by the rotors; however, this may cause problems with the stability of the platform during flight. The panacea may be a pumped metering system with input outside the platform, but this also increases the weight of the platform. Therefore, the most common practice in the literature is to place the measuring system centrally, elevated above the robot, as was done in this work. Given the large increase in interest in gas detection applications and research with flying robots, the authors predict that the specially designed new sensors will bring significant benefits and will be an important area for future research.

Based on the examples cited, some research gaps can be identified, related to, i.e., the analysis of a single robot configuration and no experimental verification of the calculations made (model calibration). Other deficiencies are related to the analysis of commercial robot solutions, which, due to their design, cannot easily integrate a measurement system for the purpose of automatically searching for the source of pollution. In cases where the sensor is placed over the robot, there are difficulties in measuring when the robot is hovering over a source of pollution. Particulate matter was also not taken into account in the simulation tests.

The aim of the work was to model the aerodynamic field around the rotors of selected types of flying robots. On this basis, the disturbance of the natural flow field caused by the rotors was estimated. Estimation allows the correct design of the particulate measurement system to search for the source of contamination. Performing such an analysis is necessary for the robot to fulfill its assigned function of locating sources of pollution. The CFD simulations were verified on a constructed dedicated dynamometer stand. As a result of this design process, the best rotor configuration and localization of sensors were selected and then a functional drone prototype for locating pollution sources was prepared and tested.

2. COMPUTATIONAL MODELS

The subjects of the analysis were configurations with one, two, four and finally six rotors (Fig. 1). The single rotor configuration was used to validate the simulations. The results of this model were compared with the data from the experiment. The two-rotor configuration is one arm of the octocopter, a quadrocopter with two rotors on each arm. The four and six rotor systems were directly related to the types of flying robots analyzed: quadro- and hexacopter. These are the robot configurations of the greatest practical importance. For these configurations, computational models of the flow field were built and then the velocity, pressure, and turbulence field distributions were determined. Aerodynamic phenomena around the robot rotors were analyzed in dedicated *ANSYS Fluent* fluid flow software.

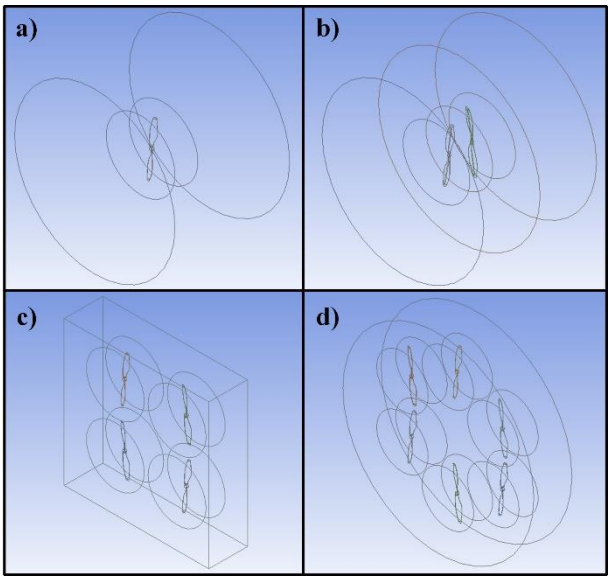

Fig. 1. Geometric models of the analyzed rotor configurations: a) one, b) two, c) four, d) six rotors

The first of the models constructed contained a single rotor (Fig. 1a). Two propellers used in the described robots were analyzed: the smaller type 1045 (10 inch diameter and 4.5 inch pitch) and the larger type 1238 (12 inch diameter and 3.8 inch pitch). The rotational speeds assumed for the calculations corresponded to the operating conditions of the discussed multirotor robots. The computational domain for these cases has the shape of a cylinder with the following dimensions: for a propeller 1045 with a diameter of 0.7 m and a height of 0.5 m, for a larger one with a diameter of 0.8 m and a height of 0.6 m. These models were verified on the basis of experimental data from a constructed dynamometer stand.

With a single-rotor model verified, it was possible to model systems with a greater number of them. The first of the more complex models was a dual-rotor system from an octocopter. This robot is in a redundant configuration, which means that it has four arms, and there are two sets of drives per arm, the top and bottom one. The total weight of this robot is 4.3 kg and is equipped with a 1238 propeller. Due to the large external dimensions and the resulting high computational complexity, it was decided to perform an analysis for

the counter-rotating configuration of the two propellers, as shown in Figure 1b. For this purpose, it was necessary to create two dynamic zones above each other, in the shape of a cylinder with a diameter of 0.36 m and a height of 0.12 m. Dynamic zones rotate at identical speeds but in opposite directions. The surroundings are a static zone, which is cylindrical in shape, 0.8 m in diameter and 0.6 m in height.

Another of the robots analyzed is a quadcopter robot equipped with four rotors, one for each arm. This robot is equipped with 1045 propellers and weighs 1.35 kg. The prepared geometrical model (Figure 1c) contains four cylindrical revolving zones with a diameter of 0.3 m and a height of 0.1 m. The robot environment is a static rectangular zone with dimensions of 0.75 m × 0.75 m × 0.2 m. The construction of the hexacopter robot (Figure 1d) is very similar. It is equipped with the same type of propeller; therefore, the same dynamic zones are adopted. Additional rotors are included, and in this case, the static zone is cylindrical in shape, 1m in diameter, and 0.2 m in height. The robot weighs 2.54 kg. In cases where a configuration of four or six rotor numbers was modeled, the prepared model covered only the closest robot environment. This is due to the fact that the arm of the measuring system must not be too far from the center of gravity of the robot, as this would significantly deteriorate the stability of the robot in the air.

First, a geometric model of the rotor (propeller) was built. In this case, the work began with 3D scans of the two described propellers. The following description of the model building process refers to a single small (1045) propeller system. Subsequent systems with a larger number of rotors were constructed in the same way. As a result of the scanning process, a file is obtained in the polygonal mesh format (STL). Such a file is not suitable for further calculations, as a solid-format model is required. Software *CATIA* was used for this task. The next step was to prepare a geometric model of the environment in which the rotor will operate. The propeller was placed in a cylinder with a diameter of 0.3 m and a height of 0.1 m. Then another cylinder, 0.7 m in diameter and 0.5 m in height, was created. A large cylinder without the volume of a small cylinder is hereinafter referred to as the static (stationary) zone. The second domain is a small cylinder without the volume of the propeller body, hereinafter referred to as the dynamic (rotational) zone.

The next step was to prepare the computational mesh. Due to the complex geometry of the propeller's body, a non-structural, non-conformal mesh was prepared. The non-structural mesh is generated automatically by the software based on defined guidelines. In particular, it was established that the element size in the revolving zone should not exceed 0.003 m (Figure 2b), and in the static 0.01 m (Figure 2a). The non-conformal mesh type means that the consistency of the mesh nodes at the domain boundaries was not guaranteed, which was difficult in the case of complex geometries and multi-rotor configurations. Additionally, in order for the modeled aerodynamic phenomena near the rotor to be considered correct, it is required that, as a result of calculations, the dimensionless distance from the wall on the rotor surface must be less than 1 over the rotor surface. This parameter of the dimensionless distance from the wall, which is determined during the modeling of flows in the vicinity of rigid walls, is called y^+. To obtain y^+ at a certain level, an additional boundary layer should be modeled. This goal is achieved by local mesh refinement (as shown in Fig. 2c) on the wall surface (here: rotor surface). The following parameters are determined: the height of the first boundary layer y, the inflation ratio, that is, the degree of increase in the height of subsequent layers, and the number of these layers. On the basis of analytical calculations, the height of the first boundary layer y was assumed to be approximately 0.006 mm. Eight

boundary layers for the rotor were assumed and the inflation ratio was assumed to be 1.2. As discussed above, it denotes the scale of growth of successive layers, starting from the boundary layer. The number of all elements in the mesh (Figure 2a) was approximately 4.4 million. Other cases were prepared in the same way, and the numbers of elements in the remaining cases were: single 1238 propeller 9.5 mln, two 1238 propellers 16.3 mln, four 1045 propellers 11.4 mln and six 1045 propellers 15.3 mln. For that mesh, the maximum value of y^+ on the rotor surface was approximately 0.74. The parameters of the grid prepared in this way were acceptable, i.a. the maximum skewness was less than 0.8. Elements with a skewness above 0.5 constituted only about 3% of all elements, which were 6 node wedges elements mostly.

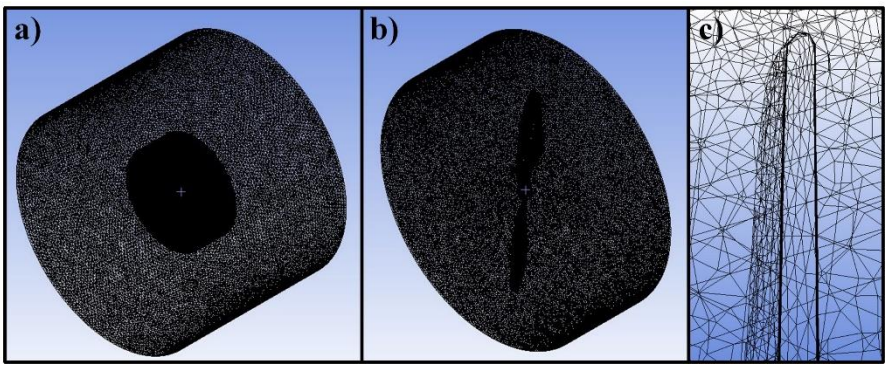

Fig. 2. Prepared mesh for the configuration with one rotor: a) whole domain, b) dynamic zone, c) close-up on the rotor boundary layer

Then the input data for the *Fluent* software was prepared, which was used to calculate the solution. In particular, the boundary conditions have been defined. The adopted boundary conditions for a configuration with one rotor are presented in Figure 3.

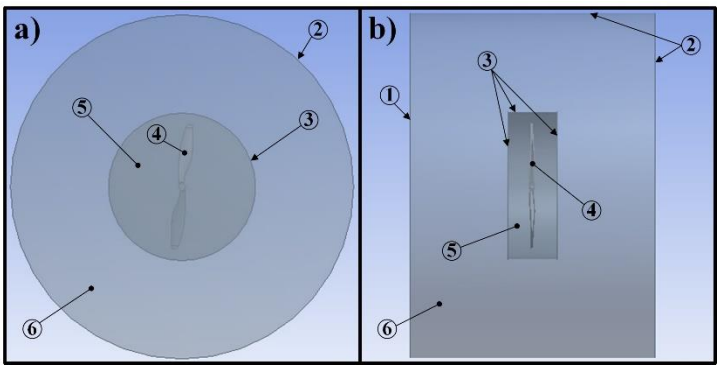

Fig. 3. Boundary conditions: a) top view, b) side view. Symbols in the drawing: 1 – *pressure-inlet* (inlet), 2 – *pressure-outlet* (outlet), 3 – *interface* (domains contact surfaces), 4 – *rotating-wall* (the surface of the propeller rigid body), 5 – dynamic zone, 6 – static zone

The upper plane (1) of the static zone cylinder (6) was defined as of *pressure-inlet* type. On the other hand, the bottom and side surfaces (2) were defined as *pressure-outlet*. The inner contact surfaces of the domain's *interfaces* (3) define the way in which the dynamic

(5) and static (6) zones interfere, that is, they define the domain contact. The propeller body itself (4) is rigid and rotates together with the rotating domain (5), so it is of the *rotating-wall* type. In addition, the axis of rotation and the rotational speed of the dynamic zone were also defined.

ANSYS Fluent solves the flow equations on a stationary frame of reference. A system with one or more rotating rotors, however, belongs to a group of problems for which it is advantageous, or even necessary, to solve equations in a non-inertial frame of reference. After activating the moving frame of reference for each of the modeled rotors of the system, the software modifies the equations of motion to consider the additional terms of acceleration that occur due to the transformation from stationary to moving frame of reference. In simulated multi-domain cases, it is required to specify the domain contact surfaces as interfaces. The interface definition method leads to two approximate steady-state modeling methods; these are the mixing plane model (MPM) or the multiple reference frame (MRF) approach used in this case. The MRF model is a steady-state approximation in which specific rotational speeds are assigned to each rotational zone. The flow in each moving zone is solved using the equations of the moving coordinate system. A local coordinate system transformation is performed at the interfaces between the rotating and stationary zones to allow the flow parameters in one zone to calculate flows at the boundary of an adjacent zone. In the case of a single-rotor system, it is possible to define the entire domain as rotating without separate division into rotating and static parts. This variant is known as a single reference frame (SRF) approach. However, because this work analyzed different rotor systems rotating at different rotational speeds, this approach was not used. When the equations of motion are solved in a moving frame of reference, additional conditions that appear in the momentum equations are considered to determine the acceleration of the fluid. In this case, the equations are formulated by expressing the momentum equations using absolute speeds as dependent variables in the momentum equations, which is known as absolute velocity formulation. It is also possible to use the frozen-rotor approach (Tulwin, 2019), where interfaces are also not used. However, the MRF model, although more complicated, allows easy use of the sliding-mesh (SM) method in the future. It is a more accurate method for high rotational speeds.

ANSYS Fluent (Ansys Fluent Theory Guide, 2020) solves the Navier-Stokes partial differential equations resulting from the principle of conservation of mass and momentum. If the flow is turbulent, additional transport equations are added. The mass conservation equation is written in a generalized form as follows:

$$\frac{\partial \rho}{\partial t} + \nabla \cdot (\rho \vec{u}) = S_m \tag{1}$$

where: ρ is the fluid density, $\vec{u}$ is the velocity, and S_m is the mass source. The conservation of momentum principle for a stationary frame of reference is described (Batchelor, 1967) by:

$$\frac{\partial}{\partial t}(\rho \vec{u}) + (\rho \vec{u} \cdot \nabla)\vec{u} = -\nabla p + \nabla \cdot \left(\overline{\overline{\tau}}\right) + \rho \vec{g} + \vec{F} \tag{2}$$

where: p is the static pressure and $\rho \vec{g}$ and $\vec{F}$ are the gravitational force and external forces, respectively. The stress tensor $\overline{\overline{\tau}}$ is given by:

$$\bar{\bar{\tau}} = \mu\left[\left(\nabla\vec{u} + \nabla\overrightarrow{u^T}\right) - \frac{2}{3}\nabla\cdot\vec{u}I\right] \tag{3}$$

where: μ is the kinetic viscosity, I is the unit tensor, and the second term on the right describes the volume dilation effect. This paper introduces simplifications regarding the lack of mass sources ($S_m = 0$), the lack of external forces ($F = 0$) and the constant fluid density ($\rho = const$), which simplify equations (1) and (2) in the form:

$$\nabla\cdot\vec{u} = 0 \tag{4}$$

$$\rho\left[\frac{\partial\vec{u}}{\partial t} + (\vec{u}\cdot\nabla)\vec{u}\right] = -\nabla p + \nabla\cdot\left(\bar{\bar{\tau}}\right) + \rho\vec{g} \tag{5}$$

Due to the necessity of solving these equations numerically, the finite-volume method, namely its RANS variant (Reynolds-Averaged Navier-Stokes), was used to determine the approximate solution. In this method, the solution variables in instantaneous (exact) Navier-Stokes equations are broken down into mean components (averaged in space or averaged over time) and unaveraged variables. For velocity u and scalar parameters ϕ this can be written as:

$$u_i(x_i,t) = \overline{u}_i(x_i) + u_i'(x_i,t), \quad \phi(x_i,t) = \overline{\phi}(x_i) + \phi'(x_i,t) \tag{6}$$

where: $\bar{u}_i$ and u_i' are respectively the mean and time-varying velocity components in three directions ($i = 1,2,3$), and $\overline{\phi}$ and ϕ' are the mean and time-varying components of scalar quantities such as pressure, energy or intensity. The turbulence intensity is a very useful metric for characterizing turbulence and is defined as the ratio of the root mean square of the velocity fluctuations to the mean flow velocity (Rodriguez, 2019). If the turbulent energy *k* is known the turbulence intensity can be computed on its basis (Ansys Fluent Theory Guide, 2020).

The standard model of *k-ω* in *Ansys Fluent* (Ansys Fluent Theory Guide, 2020; Romik & Czajka, 2022) is based on the model proposed by Wilcox (Wilcox, 2006), which is an empirical model based on the equations of transport of the kinetic energy of turbulence (*k*) and the specific dissipation rate (*ω*). Over the years, this model has been improved by adding production conditions to both equations, which has increased the accuracy of the prediction of free shear flow. The main problem with the Wilcox model is its well-known strong sensitivity to free-stream conditions. The base model *k-ω* (BSL) was developed by Menter (Menter, 1994) and contains different modeling constants. Its unique feature is that in its formulation, the standard *k-ω* model and the transformed *k-ϵ* model are multiplied by the blending function and both models are added together. The blending function is designed to be one in an area close to the wall, which activates the standard *k-ω* model, and zero away from the surface, which activates the transformed *k-ϵ* model. Another difference is that the BSL model includes a derivative of damped cross-diffusion in the equation. The Shear-Stress Transport (SST) *k-ω* model includes all the improvements to the BSL model and also includes the principal turbulent shear stress transport in the definition of turbulent viscosity. These characteristics make the SST model (Menter, 1994) more accurate and reliable for a wider class of flows, for example, with an unfavorable pressure gradient or around the airfoil, and make it definitely better for this study than the standard and BSL models.

The last stage of the work included performing the calculations and analysis of the data obtained. In general, if there are critical errors in the modeling and model definition phases, the calculations will not converge. This can be defined as the first necessary criterion for the correctness of the calculations. After satisfying this criterion, the parameters obtained on the rotor were checked next: the resulting torque and thrust force was compared with the data from the experiment. Comparison of the thrust forces and torques values is presented in the chapter on the calculation validation. The independence of the solution from the computational mesh was also examined.

3. EXPERIMENTAL VALIDATION OF SINGLE-ROTOR MODEL

To determine the unknown parameters of the selected drive sets, it turned out that it was necessary to design, build, and prepare software for a dedicated mobile dynamometer stand. The construction of the station allowed us to identify the drive unit that will be characterized by the highest thrust force achieved. Moreover, the data obtained made it possible to verify the mathematical model of the CFD. The prepared mobile measuring station enables the collection of data necessary to determine the characteristics of the drive sets of multi-rotor robots. A drive unit is understood as a complete set consisting of a propeller, a motor, and an engine speed controller (ESC). The following design assumptions were adopted for the constructed stand, i.e., that it will enable measurements of the thrust force and torque, the propeller rotational speed and the supply voltage and the current.

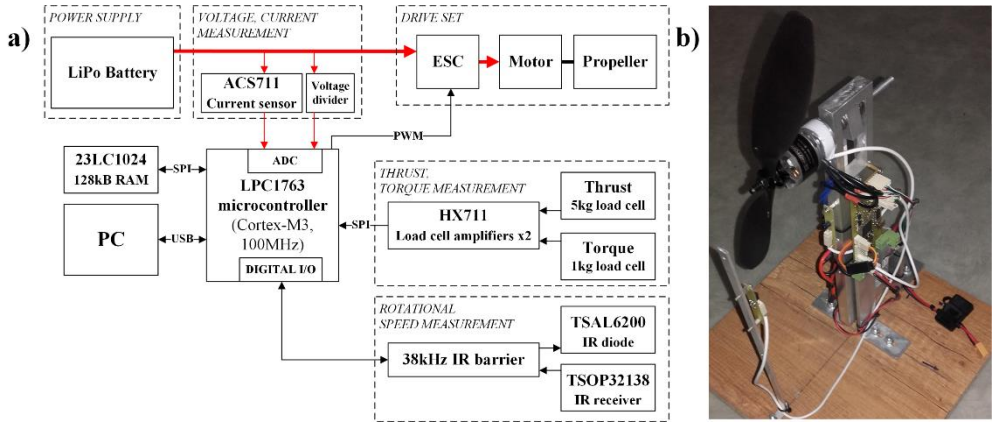

Fig. 4. Constructed dynamometer test stand: a) block diagram, b) view of the stand

The block diagram of the prepared dynamometer stand was presented in Figure 4a. The external dimensions of the entire stand (Figure 4b) are 0.3 m × 0.3 m × 0.34 m. The main control element of the electronic part of the system is the NXP LPC1763 microcontroller, which performs the measurement and control function of the entire stand. Dedicated 24bit HX711 digital scale amplifiers were used to amplify and digitize the weak signal from strain gauge beams. The motor current was measured using a ACS711 (25 A max) Hall effect current\voltage converter. Supply voltage measurements and voltage measurements from a current sensor were carried out using the microcontroller internal ADC converter. Measurement of the rotational speed of the propeller is carried out with the help of an optical

barrier. The special structure of the barrier eliminates the influence of the flickering light sources present in the room on measuring the propeller rotation speed. The optical barrier can be mounted in three different positions, thus adjusting it to the size of the mounted propeller. Measurement data are stored in an additional 23LC1024, 128 kB RAM memory. The system can communicate with a PC using the integrated USB\UART converter. These were additional technical issues that ensured the integrity of the measurement data. The stand is equipped with additional necessary safety measures. It is possible to quickly disconnect the power in the events of the internal microcontroller or PC software crashing and loss of communication with the PC. All internal microcontroller software that manages low-level functions of the station was prepared in C language. The program was prepared at a low level to obtain the highest efficiency of collecting and processing measurement data. The PC-side software that cooperates with the station was prepared in C++.

The Gefman 1045 propeller was tested with the Emax MT2213 motor, a 30A Emax ESC with a LiPo 11.1V (3S) battery. The Gefman 1238 was tested with the Emax MT2814 motor, a 40A DYS ESC with a LiPo 14.8V (4S) battery. The batteries were fully charged before measurements. Other propellers of the same type were also examined, but the presented ones were characterized by the largest thrust.

The motor with a propeller, which shaft is rotating at ω, generates a torque of M and a thrust force F, while it draws the power of P. Both the thrust force F and the torque M generated are proportional to the square, and the power P to the cube of rotational speed (Glauert, 1935). Therefore, this can be expressed as the following equations:

$$F = k\omega^2, \quad M = b\omega^2, \quad P = p\omega^3 \tag{7}$$

where: k, b, p – thrust force, torque, and power constants, respectively. These are not usually given by the manufacturer, so they were designated on the prepared dynamometer stand. In cases where the robot moves at low speeds or a steady state is analyzed when the robot is in a hover state, the influence of additional factors, such as motor shaft inertia, can be omitted. Typically, for the propulsion of analyzed robots, a dedicated brushless DC motors with a small moment of rotor inertia are used.

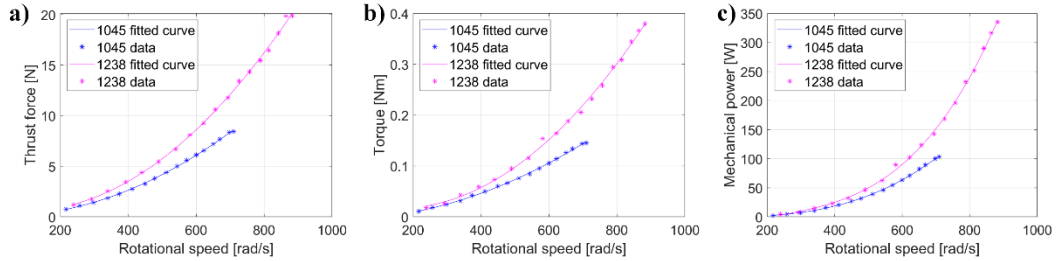

Fig. 5. Determined characteristics for both rotors: a) thrust force, b) torque, c) mechanical power

In Figure 5 the characteristics determined as a function of the rotational speed of the rotor are presented. Mechanical power was determined as the product of torque and rotor speed. On the basis of these data, a polynomial approximation could be performed, which was also presented in the chart. In the case of the thrust force and torque, a second-order polynomial was fitted, for power, the third order. The determination coefficient R^2 of these approximation functions exceeded 0.99.

On the basis of the experimental data, the CFD thrust forces and torques can be verified. The results obtained for all cases, along with the data from the experiment, are presented in Table 1. Obtaining similar results regarding these values for different meshes allowed us to state that the independence of the solution from the computational mesh was obtained.

Tab. 1. The CFD and experimental data for the single-rotor configurations analyzed

Rotor type	**1045**						**1238**		
Rotational speed [rad/s]	421.92			481.50			438.25		
	CFD	Exp.	Diff. [%]	CFD	Exp.	Diff. [%]	CFD	Exp.	Diff. [%]
Thrust force [N]	2.90	2.94	1.36	3.78	3.86	2.07	3.94	4.29	8.16
Torque [Nm]	0.047	0.052	9.62	0.061	0.068	10.29	0.061	0.071	14.08
Mechanical power [W]	19.83	21.79	9.00	29.37	32.67	10.10	26.73	33.17	19.42

As shown in Table 1, the differences between the data from the model and those from the experiment for a smaller rotor did not exceed about 10%. For a larger rotor it was around 19.5%, however, this was concerning mechanical power. For force and torque, these differences were approximately 8% and 14%, respectively. The sources of these differences can be sought primarily in: reproduction of the propeller model in the process of reverse engineering, determining engine parameters, or in general the numeric model itself. However, such small differences can be considered irrelevant, and the calculations were considered accurate enough. Moreover, the measured electric power, determined as the product of the supply voltage and current, confirmed the correct methodology of the mechanical power measurement. The estimated losses were considered in the validation.

4. COMPUTATIONAL RESULTS FROM MULTI-ROTOR MODELS

With a calibrated model for a single-rotor configuration, it was possible to verify the calculations for configurations with more than one rotor. First, the configuration with a single larger (1238) with the two rotors was compared. The results obtained were combined in Table 2. The following nomenclature was used here: *L* – left, *R* – right rotating propeller.

Tab. 2. Comparison of configurations with one and two rotors based on the CFD data

Configuration	**Single (L)**	**Dual**		
		Top (L)	Bottom (R)	Sum
Thrust force [N]	3.94	3.66	2.11	5.77
Torque [Nm]	-0.061	-0.060	0.050	-0.010
Mechanical power [W]	26.73	26.30	21.91	48.21

According to Table 2 it should be stated that the rotors working in the column generate unequal thrust forces and torques. When comparing the data with those of a single independent rotor, the top rotor in the column generates 93% of the force and 98% of the torque. For the bottom one, these amounted to only 53% and 81%, respectively. In other

words, the bottom rotor generates only 37% of the total thrust force for the entire column. When it comes to the generated moment, it is 11% smaller for that rotor. This is primarily due to the fact that the bottom propeller is already powered by pre-accelerated air by the top one. In terms of power, the column requires approximately 90% of the power compared to two independent single rotors, generating a thrust force of 73% at the same time. The verification of the four- and six-rotor configuration was carried out in the same way. Due to the similarity of these cases, only the data for a six-rotor configuration will be presented. The results obtained are presented in Table 3.

Tab. 3. Thrust forces and torques of each rotor in the six-rotor configuration

Rotor	1 (L)	2 (R)	3 (L)	4 (R)	5 (L)	6 (R)	Sum
Thrust force [N]	3.36	3.38	3.40	3.43	3.38	3.39	20.34
Torque [Nm]	-0.058	0.058	-0.057	-0.058	-0.059	0.059	0.001

As presented in Table 3, both the thrust forces and the torques generated by each of the rotors are similar in value. Compared to a single-rotor system (3.78 N thrust force, 0.061 Nm torque), lower values were obtained. In the case of forces, the result was about 10% smaller, in the case of moments about 5% smaller. It is related to the mutual influence of the working rotors on each other.

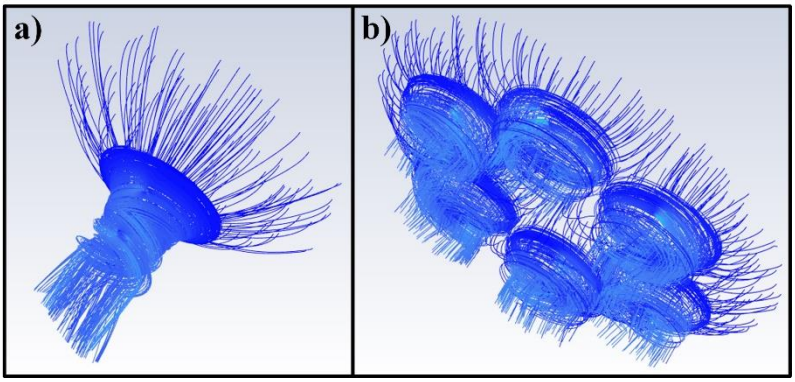

Fig. 6. Fluid flow velocity streamlines for: a) one dual, b) six single rotors configurations

Next, it was also possible to determine additional data, which was difficult to determine experimentally. These were the fluid flow velocity streamlines and the velocity, pressure (Figure 7) and the turbulence intensity field distributions. The streamlines for selected systems, colored depending on the velocity of the particles, are presented in Figure 6.

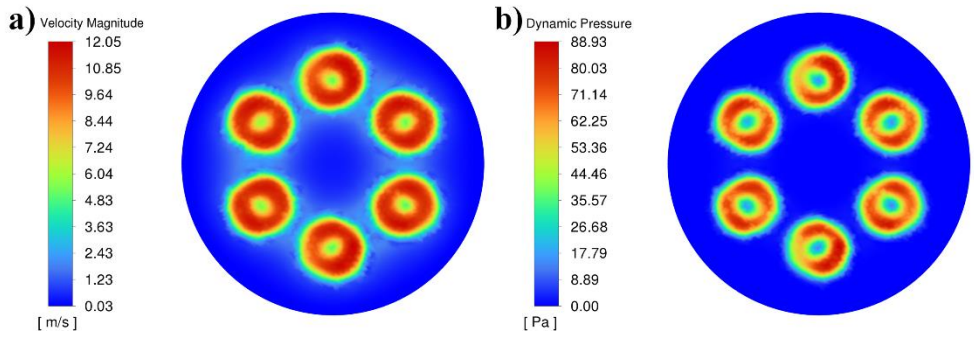

Fig. 7. The six rotors' configurations – outlet side: a) velocity magnitude, b) dynamic pressure

As can be seen in Figure 7 for the six-rotor configuration, the air velocities on the outlet side at the boundary of the computational domain reached a value of approximately 12 m/s, while the dynamic pressure was approximately 89 Pa. With these data, the following approach was determined to compare the analyzed systems. For each of them, in the transverse sections (parallel to the rotor plane) two planes were located 0.05 m and 0.1 m below the rotor plane, respectively. In the case of a two-rotor configuration, these distances are referenced to the bottom one. Then, in post-processing, using the polar coordinate system, control points were located on circles with radii increasing every 0.001 m. The coordinates of the points were selected so that the angular resolution for each radius was constant and amounted to 0.0013 radians (i.e. maintaining a constant number of 500 points on circle). At all points, total flow velocities and turbulence intensities were read and exported to the *Matlab* software, where their maximum values for each radius were determined and presented in Figures 8-9.

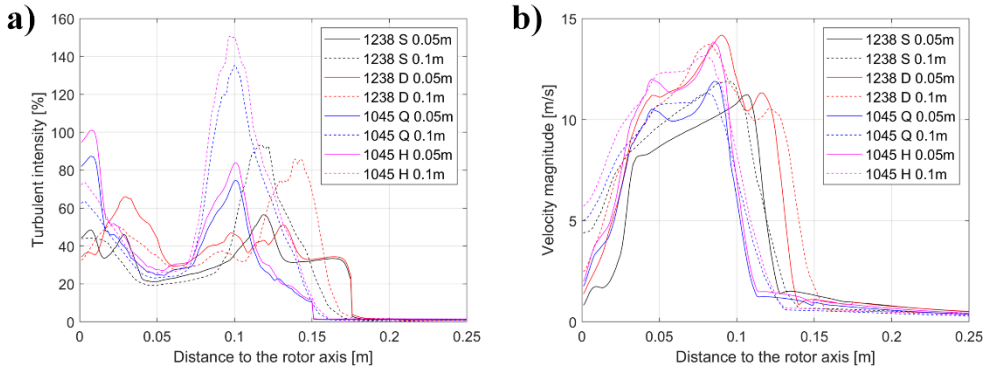

Fig. 8. Comparison of single rotors configurations: a) turbulent intensity, b) velocity magnitude

This approach made it easy to compare and evaluate each configuration. Figure 8 presents a comparison of the analyzed systems with one and two rotors in terms of turbulence intensity and flow velocity. Based on these data, it is possible to adopt a criterion that will enable the indication of the correct distance from the rotor, assuming a constant (less than) value of the flow velocity or the intensity of turbulence. The following nomenclature is used here: *1045 Q*, *1045 H* - smaller rotor for the operating conditions of a: four and six rotor

robots, respectively, *1238 S*, *1238 D* – larger rotor in a single and double arrangement, respectively. Based on these figures, it should be noted that for a cross section at a larger distance from the rotor plane, the flow velocity is slightly decreasing. In particular, for the configuration of two rotors, increased values are observed at a greater distance from the rotor.

From these results, it might be concluded that the configuration with a larger rotor is characterized by a smaller intensity of turbulence. However, the distances given in the case of this configuration are too close to the rotor, and thus there is no visible comprehensive development of the disturbed field in these figures. In addition, in the case of a system of two rotors, the defined distances are under the bottom rotor. Therefore, for a larger rotor, a cross section of 0.1 m should be compared with a cross section of 0.05 m.

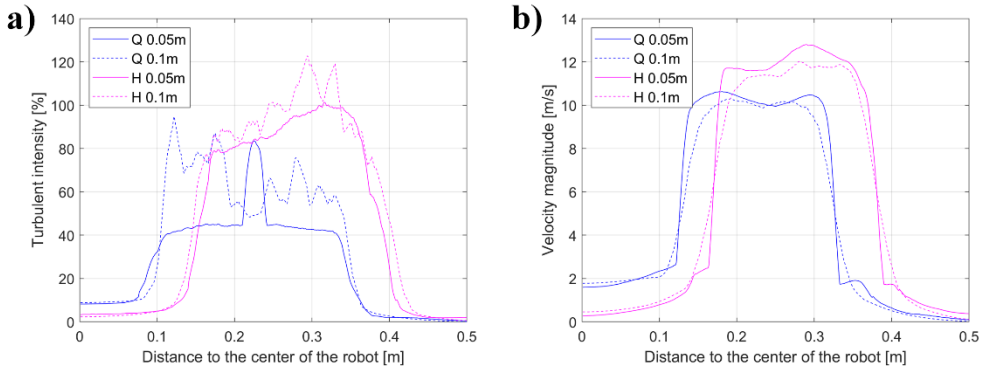

Fig. 9. Comparison of multi rotors configurations: a) turbulent intensity, b) velocity magnitude

It should be noted (Figure 8a) that the intensity of the turbulence quickly drops to a small value of about 2–3% for a smaller rotor for a distance of 0.15 m, while for the larger one it is around 0.175 m. This is because these distances correspond to the length of the propeller blade. For velocities (Figure 8b), they reach maximum values at a distance of about 0.09 m from the center of the propeller. In Figure 9 the same data for configurations with four rotors (marked *Q*), and six rotors (marked *H*) were presented. In this case, these values were determined in relation to the center of the robot.

Based on these, it can be concluded that in the case of a six-rotor configuration, both the turbulence intensity and the flow velocity are higher compared to the four-rotor configuration. However, in the case of a four-rotor configuration, these parameters closer to the geometric center of the robot are higher. This is because the distances between the rotors in the case of a quadrocopter robot are smaller. Therefore, if sensors were placed underneath the robot, a configuration with more rotors would be more appropriate. Taking into account the intensity of the turbulence, the observed small values are 0.4 m and 0.45 m, respectively, for the four- and six-rotor configurations. Figure 10 shows the six-rotor robot final design.

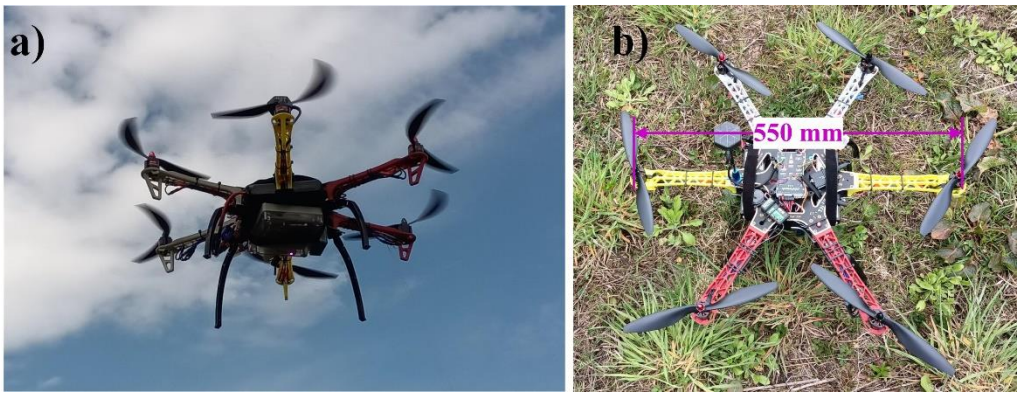

Fig. 10. Final design of six rotor robot: a) during the flight, b) on the ground

5. CONCLUSIONS

In conclusion, an analysis was carried out for selected rotor configurations of multirotor flying robots of the greatest practical importance. On the basis of the workflow presented, an analysis can be performed for any rotor configuration. The results obtained from computer models allow both to improve the design of the robot's measurement system and to improve control, which will also allow for more accurate and faster localization of pollution sources.

The analyzed configurations, among others, were characterized based on the turbulence intensity and flow velocity data. In this way, it was possible to compare and choose the most appropriate configuration. The configuration chosen for future work was a six-rotor robot. Other, additional practical considerations also decided on that choice. That is, for tests with the sensors mounted on the extended arm, the most suitable configuration is the one with more than four rotors. It not only provides redundancy, but allows one to carry larger masses. The configuration with eight rotors introduces a much larger flow-field disorder. Additional factors should be taken into account, such as the smaller thrust force of the dual rotor configuration compared to two independent rotors.

When comparing the values of the maximum parameters given in the cases of four and six rotors, the larger of them were characterized by about 29.5% higher turbulence intensity and 20.4% higher flow velocity. However, for the four-rotor configuration, the magnitudes of these flow parameters closer to the geometric of the robot are greater. When comparing data at a distance of 0.06 m from the center, the flow velocity is about 3.16 times higher and the intensity of turbulence about 2.42 times higher. This is due to the fact that the distances between the rotors of this configuration are smaller. Therefore, when locating the measuring system under the robot, the configuration with more rotors is more suitable.

The dedicated and prepared dynamometer stand allowed not only to verify the CFD computer models but also to determine the characteristics of thrust force, torque, and mechanical power. It enabled a quick and automated way to collect the necessary data. By comparing the thrust force data, itself, the largest difference between the model and the experiment value was about 8%. This value has occurred for the larger of the propellers analyzed, in the case of a smaller rotor it was only about 2%. The biggest difference occurred for the determined mechanical power. The differences in the case of a smaller rotor were at

about 10% levels, the higher at about 19%. When comparing the configuration of six smaller rotors with a single system of the same type, the differences amounted to about 5%. The biggest differences occurred for the dual rotor system; however, it is difficult to make a comparison here at the current stage because this configuration was not measured on the dynamometer station. However, in each case, these results can be considered accurate enough, and the modeling process is considered correct.

In future work, more complex simulations should be performed, including both the robot body and the particulate matter in the flow field. Furthermore, the configuration of eight rotors could be taken into account, where single rotors are arranged on eight individual robot arms, and not in a dual configuration on four arms. However, this type of robot is characterized by significant large external dimensions, which is why it is less practical. Moreover, in subsequent studies, it is planned to perform additional calculations for the SRF or frozen-rotor approaches without interfaces and SM calculations, so that the obtained results can be compared. The extended model should also have a larger computing domain and take into account the body of the robot and the particulate matter.

Author Contributions

Conceptualization, methodology, validation, and formal analysis, G.S. and R.F.; investigation, software, resources, data curation, visualization, and writing - original draft preparation, G.S.; writing – review and editing, R.F. All authors have read and agreed to the published version of the manuscript.

Funding

This research was supported by National Subvention No. 16.16.130.942.

Acknowledgments

This research was supported in part by PLGrid Infrastructure.

Conflicts of Interest

The authors declare no conflict of interests.

REFERENCES

Alvarado, M., Gonzalez, F., Erskine, P., Cliff, D., & Heuff, D. (2017). A Methodology to Monitor Airborne PM10 Dust Particles Using a Small Unmanned Aerial Vehicle. *Sensors*, *17*(2), 343. https://doi.org/10.3390/s17020343

Ansys Fluent Theory Guide. Release 2020 R1, ANSYS Inc.

Batchelor, G. K. (1967). *An Introduction to Fluid Dynamics*. Cambridge Univ. Press.

Burgués, J., Hernández, V., Lilienthal, A., & Marco, S. (2019). Smelling Nano Aerial Vehicle for Gas Source Localization and Mapping. *Sensors*, *19*(3), 478. https://doi.org/10.3390/s19030478

Chang, J. H., Chen, Y. Y., & Huang, Y. M. (2018). Design and implementation of an ambient data collection mechanism based on a quadcopter. *Proceedings – 2018 1st International Cognitive Cities Conference, IC3 2018* (pp. 32–36). IEEE. https://doi.org/10.1109/IC3.2018.00017

Chen, J., Scircle, A., Black, O., Cizdziel, J., Watson, N., Wevill, D., & Zhou, Y. (2018). On the use of multicopters for sampling and analysis of volatile organic compounds in the air by adsorption/thermal desorption GC-MS. *Air Qual Atmos Health*, *11*, 835–842. https://doi.org/10.1007/s11869-018-0588-y

Cheng, W. H., Hsieh, T. S., Chu, C. M., Chiang, C. C., & Yuan, C. S. (2019). Application of a Telescoping Microextraction Needle Trap Sampling Device on a Drone to Extract Airborne Organic Vapors. *Aerosol Air Qual. Res.*, *19*, 1593–1601. https://doi.org/10.4209/aaqr.2019.04.0183

Chiang, Y. L., Wang, J. C., Sun, C. H., Wen, T. H., Juang, J. Y., & Jiang, J. A. (2020). Mobile Measurement of Particulate Matter Concentrations on Urban Streets: System Development and Field Verification. *IEEE Access*, *8*, 197617–197629. http://doi.org/10.1109/ACCESS.2020.3034489

Chunithipaisan, S., Panyametheekul, S., Pumrin, S., Tanaksaranond, G., & Ngamsritrakul, T. (2018). Particulate Matter Monitoring Using Inexpensive Sensors and Internet GIS: A Case Study in Nan, Thailand. *Engineering Journal*, *22*, 25–37. http://doi.org/10.4186/ej.2018.22.2.25

Ciesielka, W., & Suchanek, G. (2019). Modelling and simulation tests of a quadrocopter flying robot. *New Trends in Production Engineering*, *2*(1), 486–495. http://doi.org/10.2478/ntpe-2019-0052

Dieu Hien, V. T., Lin, C., Thanh, V. C., Kim Oanh, N. T., Thanh, B. X., Weng, C. E., Yuan, C. S., & Rene, E. R. (2019). An overview of the development of vertical sampling technologies for ambient volatile organic compounds (VOCs). *Journal of Environmental Management*, *247*, 401–412. http://doi.org/10.1016/j.jenvman.2019.06.090

Faraz, A., Pushpendra, K., Yasar, K., & Pravin, P. P. (2020). Flow and Structural Analysis of a Quadcopter UAV. *International Journal of Advanced Research in Engineering and Technology (IJARET)*, *11*(8), 880–888. http://doi.org/10.34218/IJARET.11.8.2020.086

Glauert, H. (1935). *Airplane Propellers. In: Aerodynamic Theory*. Springer Heidelberg. https://doi.org/10.1007/978-3-642-91487-4_3

Gu, Q. R., Michanowicz, D., & Jia, C. (2018). Developing a Modular Unmanned Aerial Vehicle (UAV) Platform for Air Pollution Profiling. *Sensors*, *18*(12), 4363. https://doi.org/10.3390/s18124363

Hutchinson, M., Liu, C., Chen, W. H. (2019). Source term estimation of a hazardous airborne release using an unmanned aerial vehicle. *J Field Robotics*, *36*, 797–817. https://doi.org/10.1002/rob.21844

Landolsi, T., Sagahyroon, A., Mirza, M., Aref, O., Maki, F., & Maki, S. (2018). Pollution monitoring system using position-aware drones with 802.11 Ad-Hoc networks. *2018 IEEE Conference on Wireless Sensors, ICWiSe 2018* (pp. 40–43). IEEE. https://doi.org/10.1109/ICWISE.2018.8633285

Luo, B., Meng, Q., Wang, J., & Ma, S. (2016). A numerical model to simulate the aerodynamic olfactory effect of the gas-sensitive UAV. 2*016 12th World Congress on Intelligent Control and Automation (WCICA)* (pp. 3295–3300). IEEE. http://doi.org/10.1109/WCICA.2016.7578639

Mayuga, G. P., Favila, C., Oppus, C., Macatulad, E., & Lim, L. H. (2018). Airborne Particulate Matter Monitoring Using UAVs for Smart Cities and Urban Areas. *TENCON 2018 - 2018 IEEE Region 10 Conference* (pp. 1398–1402). IEEE. http://doi.org/10.1109/TENCON.2018.8650293

Menter, F. R. (1994). Two-Equation, Eddy-Viscosity, Turbulence Models for Engineering Applications. *AIAA Journal*, *32*, 1598–1605. https://doi.org/10.2514/3.12149

Nagy, A., & Jahn, I. (2019). Advanced Data Acquisition System for Wind Energy Applications. *Periodica Polytechnica Transportation Engineering*, *47*(2), 124–130. https://doi.org/10.3311/PPtr.11515

Ni, J., Yao, L., Zhang, J., Cao, W., Zhu, Y., & Tai, X. (2017). Development of an Unmanned Aerial Vehicle-Borne Crop-Growth Monitoring System. *Sensors*, *17*(3), 502. http://dx.doi.org/10.3390/s17030502

Parra, P. H. G., Angulo, M. V. D., & Gaona, G. E. E. (2018). CFD Analysis of two and four blades for multirotor Unmanned Aerial Vehicle. *2018 IEEE 2nd Colombian Conference on Robotics and Automation (CCRA)* (pp. 1–6). IEEE. http://doi.org/10.1109/CCRA.2018.8588130

Rodriguez, S. (2019). *Applied Computational Fluid Dynamics and Turbulence Modeling: Practical Tools, Tips and Techniques*. Springer Cham. https://doi.org/10.1007/978-3-030-28691-0

Romik, D., & Czajka, I. (2022). Numerical Investigation of the Sensitivity of the Acoustic Power Level to Changes in Selected Design Parameters of an Axial Fan. *Energies*, *15*(4), 1357. https://doi.org/10.3390/en15041357

Smith, B., John, G., Stark, B., Christensen, L. E., & Chen, Y. (2016). Applicability of unmanned aerial systems for leak detection. *2016 International Conference on Unmanned Aircraft Systems (ICUAS)* (pp. 1220–1227). IEEE. http://doi.org/10.1109/ICUAS.2016.7502635

Suchanek, G., Wołoszyn, J., & Gołaś, A. (2022). Evaluation of Selected Algorithms for Air Pollution Source Localisation Using Drones. *Sustainability*, *14*(5), 3049. https://doi.org/10.3390/su14053049

Tulwin, T. (2019). Low Reynolds Number Rotor Blade Aerodynamic Analysis. *MATEC Web of Conferences*, *252*, 04006. https://doi.org/10.1051/matecconf/201925204006

Villa, T., Salimi, F., Morton, K., Morawska, L., & Gonzalez, F. (2016). Development and Validation of a UAV Based System for Air Pollution Measurements. *Sensors*, *16*(12), 2202. https://doi.org/10.3390/s16122202

Wang, D., Wang, Z., Peng, Z. R., & Wang, D. (2020). Using unmanned aerial vehicle to investigate the vertical distribution of fine particulate matter. *International Journal of Environmental Science and Technology*, *17*, 219–230. https://doi.org/10.1007/s13762-019-02449-6

Wang, Q. (2019). Real-time Atmospheric Monitoring of Urban Air Pollution Using Unmanned Aerial Vehicles. *WIT Transactions on Ecology and the Environment*, *236*, 79–88. http://doi.org/10.2495/AIR190081

Wilcox, D. C. (2006). *Turbulence Modeling for CFD (Third Edition)*. D C W Industries.